Supplemental Information

Formation and Dynamics of Electron-irradiation-induced Defects in Hexagonal

Boron Nitride at Elevated Temperatures

Thang Pham[a,b,d,e], Ashley L. Gibb[a,c,d,e], Zhenglu Li[a,d], S. Matt Gilbert[a,c,d], Chengyu Song[f],

Steven G. Louie[a,d], and Alex Zettl[a,c,d*]

[a] Department of Physics, University of California at Berkeley, Berkeley, CA 94720,

USA

[b] Department of Materials Science and Engineering, University of California at

Berkeley, Berkeley, CA 94720, USA.

[c] Department of Chemistry, University of California at Berkeley, Berkeley, CA 94720,

USA

[d] Materials Sciences Division, Lawrence Berkeley National Laboratory, Berkeley, CA

94720 USA.

[e] Kavli Energy NanoSciences Institute at the University of California, Berkeley and

the Lawrence Berkeley National Laboratory, Berkeley, CA 94720 USA.

[f] Molecular Foundry, Lawrence Berkeley National Laboratory, Berkeley, CA 94720

USA.

Corresponding author: azettl@berkeley.edu

h-BN synthesis: h-BN was synthesized by using a carbothermic reduction reaction between highly oriented pyrolitic graphite (HOPG) flakes (as carbon template), boron oxide powder (as boron source) and nitrogen gas (as nitrogen source) at high temperature (1600 – 1800 °C) in an induction heating furnace. The schematic of the experiment setup can be found in Ref. 1 and 2.[1,2] In summary, at high temperature boron oxide vapor and nitrogen gas were mixed thoroughly and then reacted with HOPG by a carbothermic reduction reaction:

$$3C_{(HOPG)} + B_2O_3 + N_2 \rightarrow 2BN_{(h\text{-}BN)} + 3CO$$
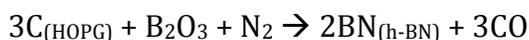
HOPG acts as a carbon template, in which carbon atoms will be substituted by boron and nitrogen atoms.[2] The as-prepared h-BN was then annealed in air at 600 – 700 °C to remove any residually non-reacted carbon. After that the samples were sonicated in iso-propanol for 30 mins and dropped cast on TEM grids for electron microscopy studies.

Initial Characterization

Figure SI1 presents a low-magnification TEM image of the as-synthesized h-BN flakes. The flakes generally consist of two to five layers and are approximately 3-5 microns in width. The inset of Fig. 1a shows corresponding selected area electron diffraction indicating high sample crystallinity. Chemical composition is confirmed by electron energy loss spectroscopy (EELS) and Raman spectroscopy. The EELS spectrum (Fig. SI1b) shows only two edges of K-B and K-N with atomic ratio approximately 1:1, as expected for pure h-BN. The Raman spectrum (Fig. SI1c) shows a prominent peak at 1366 cm^{-1} corresponding to the in-plane vibration mode

(E_{2g}) of h-BN. There is no peak in either of the EELS or Raman spectra that would indicate the presence of carbon.
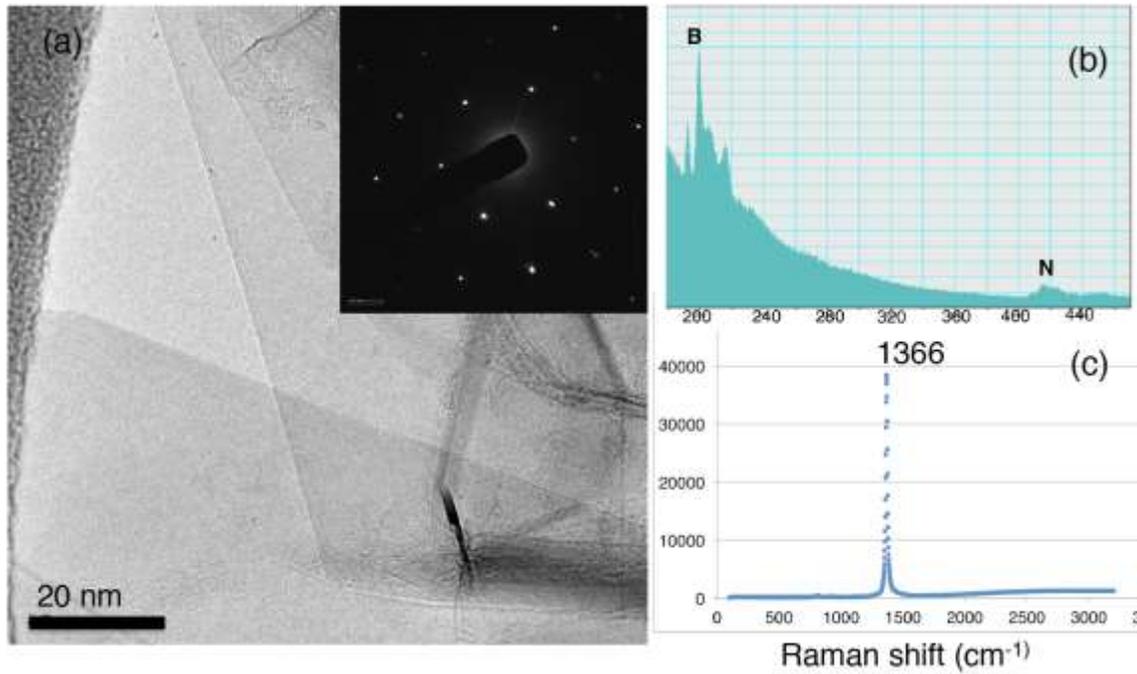
Figure SI1. (a) A TEM image of as – prepared h-BN flakes. (Inset) Selected area electron diffraction shows high crystallinity of our materials. (b) EELS and (c) Raman spectrum confirm the chemical composition of our h-BN.

Observation of hexagonal defects at different temperatures
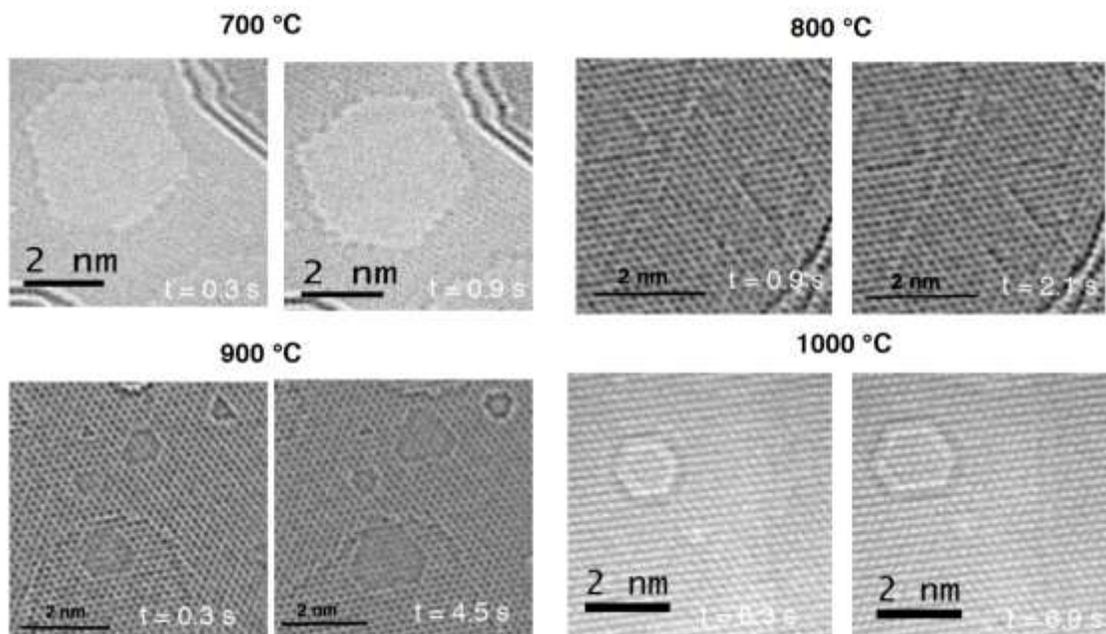
Figure SI2. HRTEM images of hexagonal defects at 700, 800, 900 and 1000°C. The time label in each image indicates when they were taken in a particular fixed-temperature time-series.

Dynamics of a hexagon defect
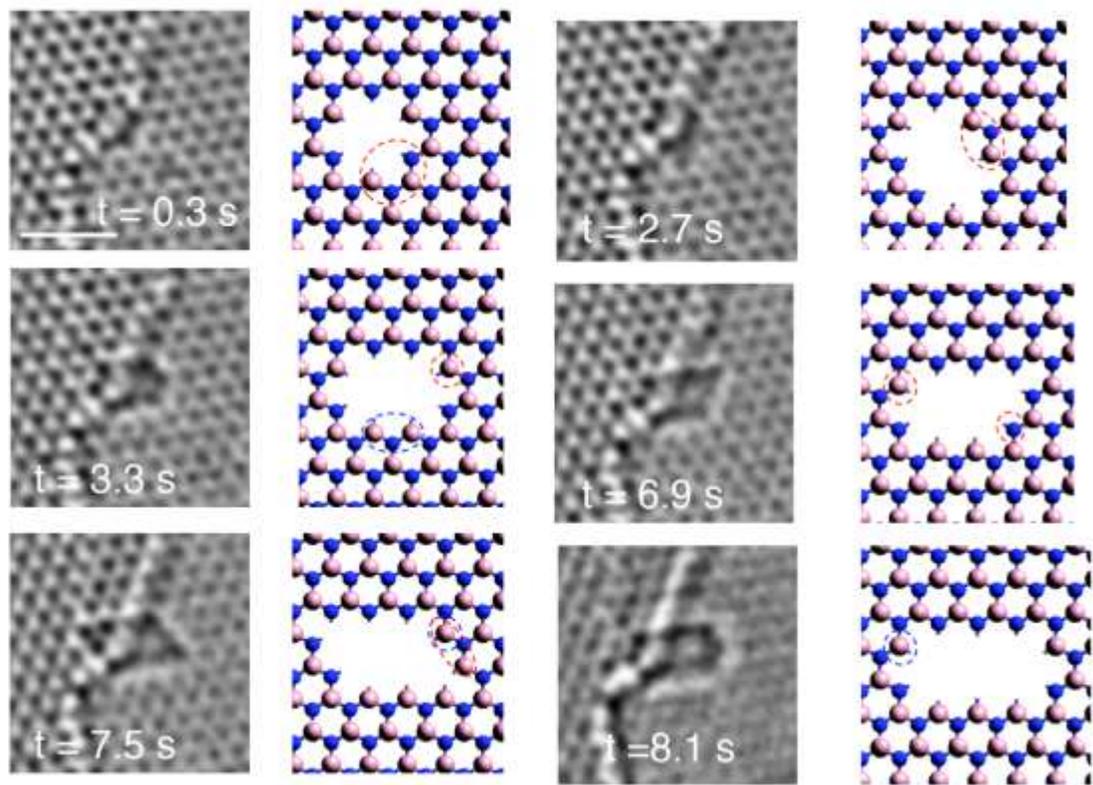
Figure SI3. Time evolution of atomic structure of a hexagon defect at 900 °C. The red dotted circle indicates atom or chain of atoms, which will be removed in the next time frame while the blue circle indicates newly added atom(s). Scale bars are 1 nm.
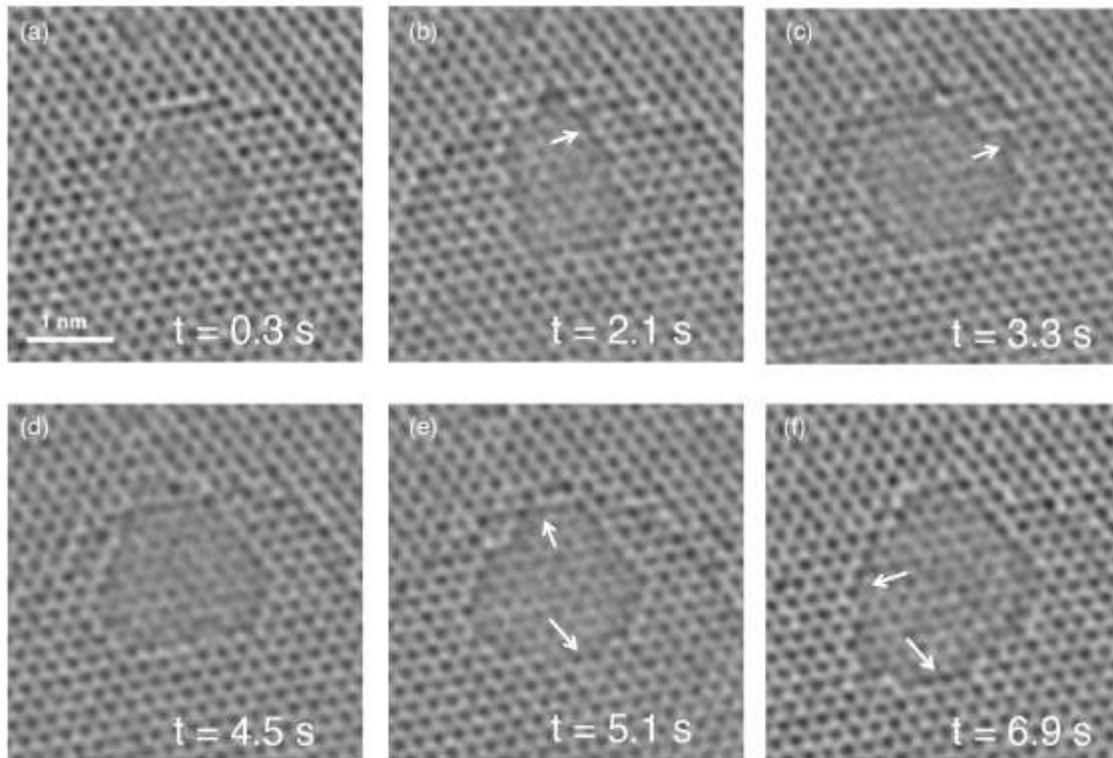
Figure SI4. HRTEM images of a hexagon defect at 900 °C. The white arrows indicate bundles of atoms, which were ejected while the defect grows.
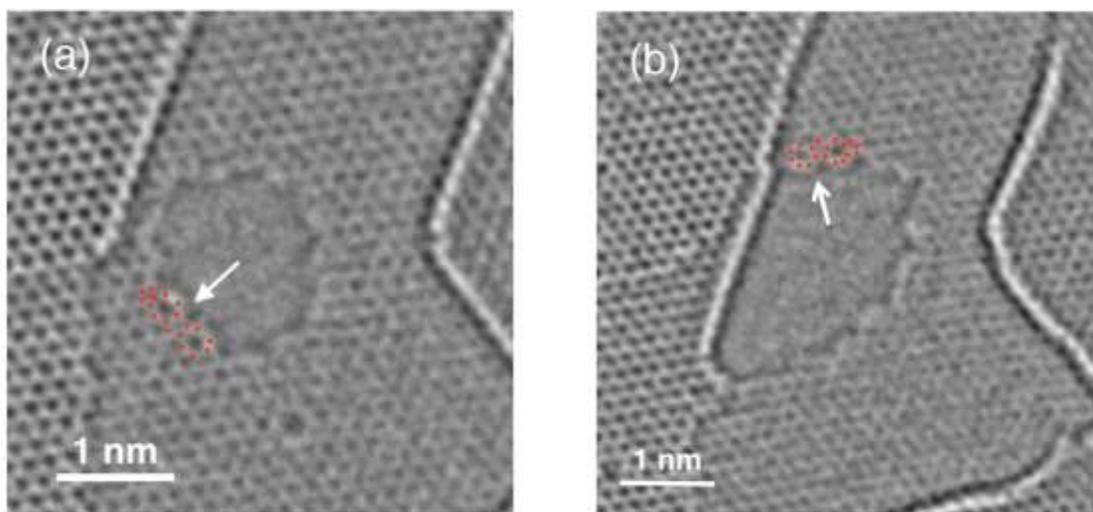
Figure SI5. Topographic defects (pentagon-heptagon (5|7) pairs) at the defect edge in h-BN (at 900 °C). Red dots illustrate atom positions and white arrows indicate topographic defects.

Topological Defects at The Inner Edges

We direct attention towards edge reconstruction of h-BN at high temperature and under electron beam irradiation. In the case of graphene, edge reconstruction from zigzag to 5|7-zigzag, edges are readily seen under electron beam irradiation.[7,8] In h-BN due to its elemental heterogeneity 5|7 topographic defects are energetically unfavorable since they involve homonuclear bonds between B-B and N-N.[9] Previous studies show the occasional presence of such defects during imaging. There is a special case[10,11] where these 5|7 defects are particularly stable, and that is at the grain boundaries of h-BN. Here the lattice strain at the grain boundaries compensates their high formation energy. However, there is no study reporting the presence of these topological defects at the edge of h-BN.[12,13] Here we clearly observe the presence of 5|7 pairs, as shown in Fig. SI5. Due to the unfavorable nature of this defect and the fast dynamics occurring at the edges, these defects usually exist in one frame and then either relax back to 6-member rings or are ejected. Further studies with shorter exposure time and a faster scanning camera might capture the dynamics of these defects and shed light on edge reconstruction in h-BN.

First-principles calculations

First-principles calculations are performed within the density functional theory using Quantum Espresso package[3]. We use a plane wave basis set with 45 Ry cutoff,

and projector augmented wave pseudopotentials under local density approximation[4]. We fully relax the lattice vectors and internal coordinates of pristine monolayer BN with 10 Å vacuum size, based on which we construct the defect structures in supercells such that the defect-defect distance in the periodic image is larger than 9 Å. We have calculated with six defect structures, as shown in Table I, that there are three types of them, i.e., triangular defects with N terminated edges (tri-N), triangular defects with B terminated edges (tri-B), and hexagonal defects with both N and B terminated edges (hex). For each type of defect, we calculate two different sizes, therefore we can extract the edge and corner energies later[5]. In the calculations of defects in supercells, we fix the lattice constant from pristine monolayer BN to mimic an environment with relatively low defect density, and fully relax the internal coordinates to let the edges and corners reconstruct.

Table SI1. Defect structures calculated in this work and their formation enthalpies ΔH under two chemical potential limits.

Defect structures	Description	Edge length (number of atoms)	ΔH (Ry), N-rich	ΔH (Ry), B-rich
tri-N-49	Triangle, 3 N terminated edges, 3 60° N-corners, hole of 28 B and 21 N	7	4.180	5.727
tri-N-64	Triangle, 3 N terminated edges, 3 60° N-corners, hole of 36 B and 28 N	8	4.816	6.584
tri-B-49	Triangle, 3 B terminated edges, 3 60° B-corners, hole of 21 B and 28 N	7	5.501	3.955
tri-B-64	Triangle, 3 B terminated edges, 3 60° B-corners, hole of 28 B and 36 N	8	6.320	4.552
hex-96	Hexagon, 3 N and 3 B terminated edges, 6 120° BN-corners, hole of	4	5.566	

	48 B and 48 N		
hex-150	Hexagon, 3 N and 3 B terminated edges, 6 120° BN-corners, hole of 75 B and 75 N	5	7.179

Table SI2. Calculated formation enthalpies for edges and corners in different defect types.

Defects	Edge ΔH (Ry / atom)		Corner ΔH (Ry / corner)	
	N-rich	B-rich	N-rich	B-rich
tri-N	0.212	0.286	-0.091	-0.091
tri-B	0.273	0.199	-0.077	-0.077
hex	0.269		-0.148	

To calculate the formation enthalpy ΔH of each defect structure, we need the information of chemical potentials, i.e. the chemical environment when the system reaches thermal equilibrium. The chemical potential of monolayer BN is denoted as μ_{BN} for 1 B atom and 1 N atom together. The chemical potentials of B and N atoms, are referenced to their elementary substances, chosen as α-boron and N_2 molecule, and denoted as μ_{0B} and μ_{0N} for per atom, respectively. In a thermal equilibrium state with dominating monolayer BN, we have a constraint[6],

$$\mu_B + \mu_N = \mu_{BN} \qquad (1)$$

Under two extreme chemical environment limits, the chemical potential of B (μ_B) and N (μ_N) can therefore be determined as follow,

$$\text{N-rich:} \quad \mu_N = \mu_{0N}, \quad \mu_{B} = \mu_{BN} - \mu_N \qquad (2)$$

$$\text{B-rich:} \quad \mu_B = \mu_{0B}, \quad \mu_{N} = \mu_{BN} - \mu_B \qquad (3)$$

In reality, the chemical potentials μ_B and μ_N can vary, but would not be out of the range defined by Eq. (2) and (3) in the thermal equilibrium states. With well-defined

chemical potentials under each chemical environment, we can calculate the

formation energy for each defect structure by using

$$\Delta H = E_{\text{supercell}}(\text{defect}) + \mu_B \times N_{\text{(missing B)}} + \mu_N \times N_{\text{(missing N)}} - E_{\text{supercell}}(\text{pristine}) \quad (4)$$

where $E_{\text{supercell}}(\text{defect})$ is the total energy of a defect structure in a supercell,

$E_{\text{supercell}}(\text{pristine})$ is the total energy of the pristine monolayer BN in the same size

supercell, $N_{\text{(missing B)}}$ and $N_{\text{(missing N)}}$ are the number of missing B and N atoms in the

formation of the defect structure (see Table SI1) from the pristine structure. The

calculated formation enthalpy for the six defect structures are listed in Table SI1.

We notice that for the hexagonal defects, the formation enthalpy is independent of

the elemental chemical potential μ_B and μ_N, because in such defects, the number of

(missing) B and N atoms are always equal, so the chemical potentials simply come

from the constraint Eq. (1). By calculating two defect structures with different sizes

of one type, we can extrapolate the edge and corner energies approximately (the

difference in formation enthalpy of two sizes gives the formation enthalpy of the

edges, and then the formation enthalpy of the corners can be derived[5]), as are listed

in Table SI2.

Videos: Dynamics and growth of defects at different temperatures

(Video 1) 500_TimeSeries1: triangle defects grow

(Video 2) 900_TimeSeries1: hexagon defects grow

(Video 3 and Video 4) 1000_TimeSeries1 and 1000_TimeSeries2: Two examples of

polygon defects grow in a manner to retain 120 ° vertices.

References:

(1)   Rousseas, M.; Goldstein, A. P.; Mickelson, W.; Worsley, M. A.; Woo, L.; Zettl, A. *ACS Nano* **2013**, *7* (10), 8540–8546.

(2)   Pham, T.; Goldstein, A. P.; Lewicki, J. P.; Kucheyev, S. O.; Wang, C.; Russell, T. P.; Worsley, M. A.; Woo, L.; Mickelson, W.; Zettl, A. *Nanoscale* **2015**, *7* (23), 10449–10458.

(3)   Giannozzi, P.; Baroni, S.; Bonini, N.; Calandra, M.; Car, R.; Cavazzoni, C.; Ceresoli, D.; Chiarotti, G. L.; Cococcioni, M.; Dabo, I. et al. *J. Phys. Condens. Matter* **2009**, *21* (39), 395502.

(4)   Perdew, J. P.; Zunger, A. *Phys. Rev. B* **1981**, *23* (10), 5048–5079.

(5)   Zhang, S. B.; Wei, S.-H. *Phys. Rev. Lett.* **2004**, *92* (8), 086102.

(6)   Schmidt, T. M.; Baierle, R. J.; Piquini, P.; Fazzio, A. *Phys. Rev. B* **2003**, *67* (11), 113407.

(7)   He, K.; Robertson, A. W.; Fan, Y.; Allen, C. S.; Lin, Y.-C.; Suenaga, K.; Kirkland, A. I.; Warner, J. H. *ACS Nano* **2015**, *9* (5), 4786–4795.

(8)   Girit, C. O.; Meyer, J. C.; Erni, R.; Rossell, M. D.; Kisielowski, C.; Yang, L.; Park, C.-H.; Crommie, M. F.; Cohen, M. L.; Louie, S. G.; Zettl, A. *Science* **2009**, *323* (5922), 1705–1708.

(9)   Cohen, M. L.; Zettl, A. *Phys. Today* **2010**, *63* (11), 34–38.

(10)   Gibb, A. L.; Alem, N.; Chen, J.-H.; Erickson, K. J.; Ciston, J.; Gautam, A.; Linck, M.; Zettl, A. *J. Am. Chem. Soc.* **2013**, *135* (18), 6758–6761.

(11)   Li, Q.; Zou, X.; Liu, M.; Sun, J.; Gao, Y.; Qi, Y.; Zhou, X.; Yakobson, B. I.; Zhang, Y.;

Liu, Z. *Nano Lett.* **2015**, *15* (9), 5804–5810.

(12)   Mukherjee, R.; Bhowmick, S. *J. Chem. Theory Comput.* **2011**, *7* (3), 720–724.

(13)   Huang, B.; Lee, H.; Gu, B.-L.; Liu, F.; Duan, W. *Nano Res.* **2011**, *5* (1), 62–72.